

Cyanostilbene-Based Vapo-Fluorochromic Supramolecular Assemblies for Reversible 3D Code Encryption

Zhao Gao,^{ab} Ze Chen,^a Yifei Han,^a and Feng Wang^{*a}

^aCAS Key Laboratory of Soft Matter Chemistry, iChEM (Collaborative Innovation Center of Chemistry for Energy Materials), Department of Polymer Science and Engineering, University of Science and Technology of China, Hefei 230026, China.
E-mail: drfwang@ustc.edu.cn.

^bShanxi Key Laboratory of Macromolecular Science and Technology, MOE Key Laboratory of Material Physics and Chemistry under Extraordinary Conditions, School of Chemistry and Chemical Engineering, Northwestern Polytechnical University, Xi'an 710072, China.

Supporting Information

1.	<i>Materials and methods</i>	S2
2.	<i>Mathematical fitting of the supramolecular assembly processes</i>	S3
3.	<i>Supramolecular assembly behaviors of 1–3</i>	S4
4.	<i>Vapo-fluorochromism of 1–2 toward smart 3D code applications</i>	S10
5.	<i>Synthetic routes to compounds 1–3</i>	S11

1. Materials and methods

Diethyl (4-nitrobenzyl)phosphonate (see Scheme S2),^{S1} compounds **5**,^{S2} **6**,^{S3} and **7**^{S4} (see Scheme S1) were synthesized according to the previously reported literatures. Other reagents and solvents used in the experiments were purchased from the commercial sources without further purification.

¹H NMR spectra were collected on a Varian Unity INOVA-300 spectrometer with TMS as the internal standard. ¹³C NMR spectra were recorded on a Varian Unity INOVA-300 spectrometer at 75 MHz. MALDI-TOF measurements were recorded on a Bruker Autoflex Speed spectrometer with DCTB as the matrix. UV–Vis spectra was recorded on a UV-1800 Shimadzu spectrometer. Solution excitation and steady-state fluorescence emission spectra were recorded on a FluoroMax-4 spectrofluorometer (Horiba Scientific). The time-resolved fluorescence lifetime experiments were performed with an Edinburgh FLS1000 transient steady-state fluorescence spectrometer. Transmission electron microscope (TEM) images were performed on a Tecnai G2 Spirit BioTWIN electron microscope (acceleration voltage: 120 kV). Dynamic light scattering (DLS) experiments were conducted on a Malvern Zeta-sizer Nano ZS Instrument.

Theoretical calculations: all of the optimized structures were performed on G09 software packages.^{S5} All of the elements were described by PBE/PBE/6-31G(d) computational method. There are no imaginary frequencies for the optimized geometries.

Inkjet printing experiments: the printing experiments were performed on a commercially available inkjet printer (HP Deskjet 2131 model) with the customized HP803 black and tri-color ink cartridges. The filled color inks from the cartridge were removed, and the cartridge was washed with ethanol, water and dried with N₂ blowing. The inks (0.5 mL) of **1–2** (1 mM) were then loaded in the clean tri-color inkjet cartridge to perform the printing experiments.

2. Mathematical fitting of the supramolecular assembly processes

2.1 Temperature-dependent supramolecular assembly process

For compounds **1**, **2**, and **3**, deeper insights into their supramolecular assembly processes are achieved by means of temperature-dependent UV–Vis spectra experiments. In terms of **1** and **2**, sigmoidal curves are obtained by plotting the fraction of aggregated species (α_{agg}) against temperature, revealing the involvement of isodesmic self-assembly mechanism. To acquire detailed thermodynamic parameters for the self-assembly processes, the normalized UV–Vis melting curves obtained by plotting α_{agg} ($\lambda = 470$ nm for **1**, and 515 nm for **2**) against temperature are fitted with the isodesmic model.^{S6} For **3**, it adopts cooperative mechanism for the supramolecular assembling process. Meijer–Schenning–Van-der-Schoot model^{S7} is employed to fit the melting curves. In detail, a non-sigmoidal curve is obtained by plotting α_{agg} against temperature at 377 nm. The detailed self-assembling thermodynamic parameters are shown in Tables S2 and S4 (*vide infra*).

2.2 Solvent-dependent supramolecular assembly process

The supramolecular assembly mechanism can be also probed *via* solvent-dependent UV–Vis measurements.^{S8} For **1** and **2**, sigmoidal denaturation curves are obtained upon plotting α_{agg} vs. the CHCl₃ volume fraction (f), respectively. In particular, α_{agg} is described by using Eq. S1:

$$\alpha_{\text{agg}} = \frac{x_{\text{tot}} - x}{x_{\text{tot}}} \quad (\text{Eq. S1})$$

x_{tot} is the dimensionless total concentration of monomers, x is the dimensionless concentration of monomers.

x_{tot} can be described by using Eq. S2:

$$x_{\text{tot}} = \sigma^{-1} \sum_{i=1}^n i(\sigma x)^i + \sigma^{n-1} \sum_{i=n+1}^{\infty} i x^i \quad (\text{Eq. S2})$$

In this equation, σ is the cooperativity parameter.

In addition, equilibrium constants (K_a) and Gibbs free energy of monomers in pure MCH (ΔG_0) are described by using Eq. S3 and S4:

$$K_a = \exp(-\Delta G_f/RT) \quad (\text{Eq. S3})$$

$$\Delta G_f = \Delta G^0 + mf \quad (\text{Eq. S4})$$

The dependence of ΔG_f on f is described by the m -value. R is the gas constant, and T is the temperature.

Solving Eq. S1–S4 using Matlab software yields the thermodynamic parameters (σ , ΔG^0 , K_e) for the solvent-dependent supramolecular assembly process.

3. Supramolecular assembly behaviors of 1–3

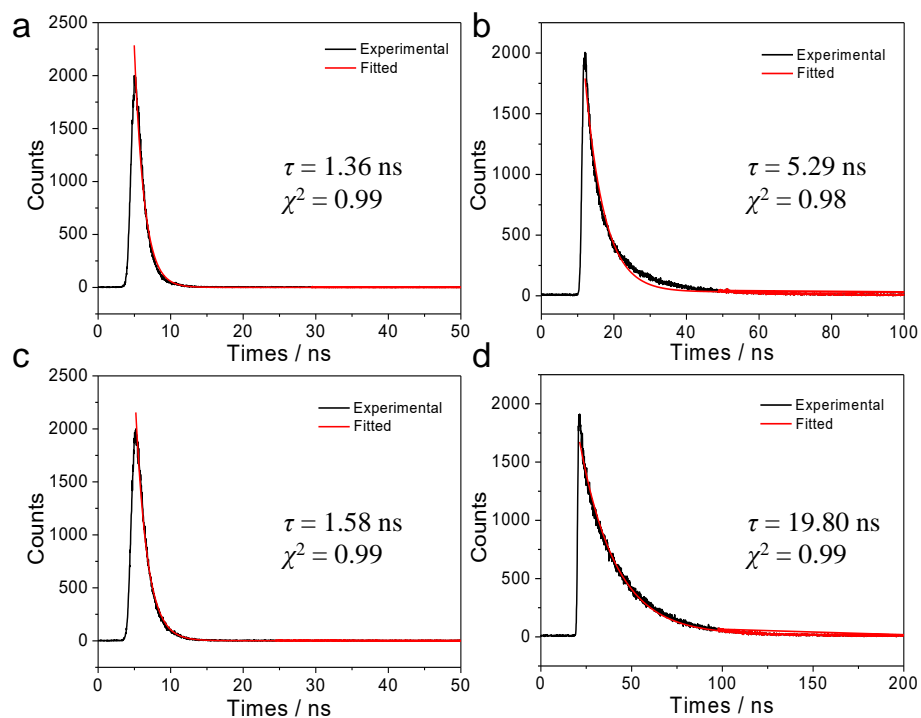


Figure S1. Fluorescence decay profiles of **1** (1.00×10^{-5} M) in (a) CHCl_3 ($\lambda = 493$ nm) and (b) MCH ($\lambda = 559$ nm), and **2** (1.00×10^{-5} M) in (c) CHCl_3 ($\lambda = 536$ nm) and (d) MCH ($\lambda = 603$ nm).

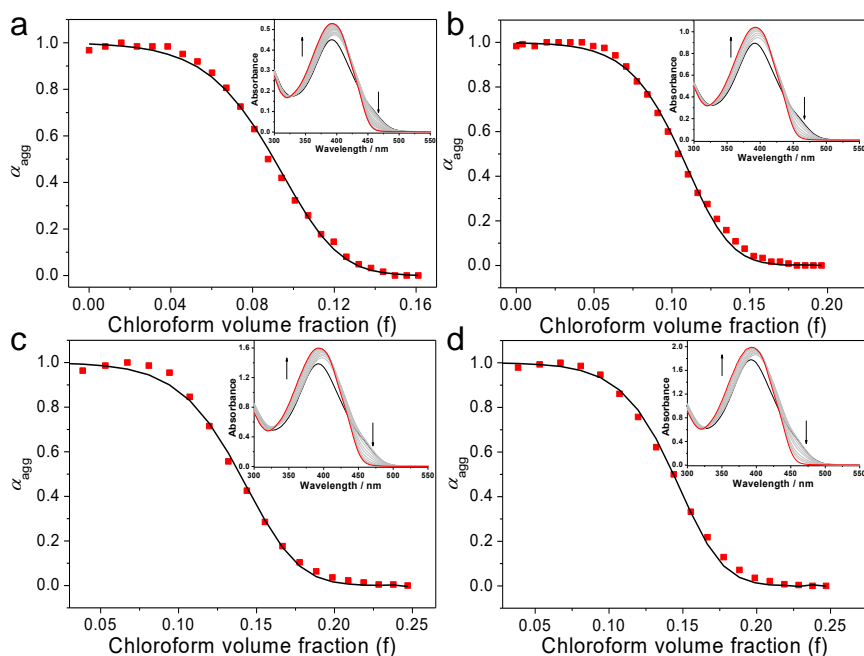


Figure S2. Degree of aggregation (α_{agg}) as a function of CHCl_3 volume fraction (f) monitored at 470 nm: a) 1.00×10^{-5} M; b) 2.00×10^{-5} M; c) 3.00×10^{-5} M; d) 4.00×10^{-5} M in MCH.

The black lines denote the respective mathematical fitting of the curve according to the solvent-dependent equilibrium model (equations S1–S4). Inset: solvent-dependent UV–Vis

absorption spectra of **1**. Arrows indicate the spectral changes upon increasing CHCl_3 volume fraction. The cooperativity parameter (σ) is determined to be 1, demonstrating the involvement of isodesmic mechanism for the self-assembly process of **1**. The detailed thermodynamic parameters are shown in Table S1.

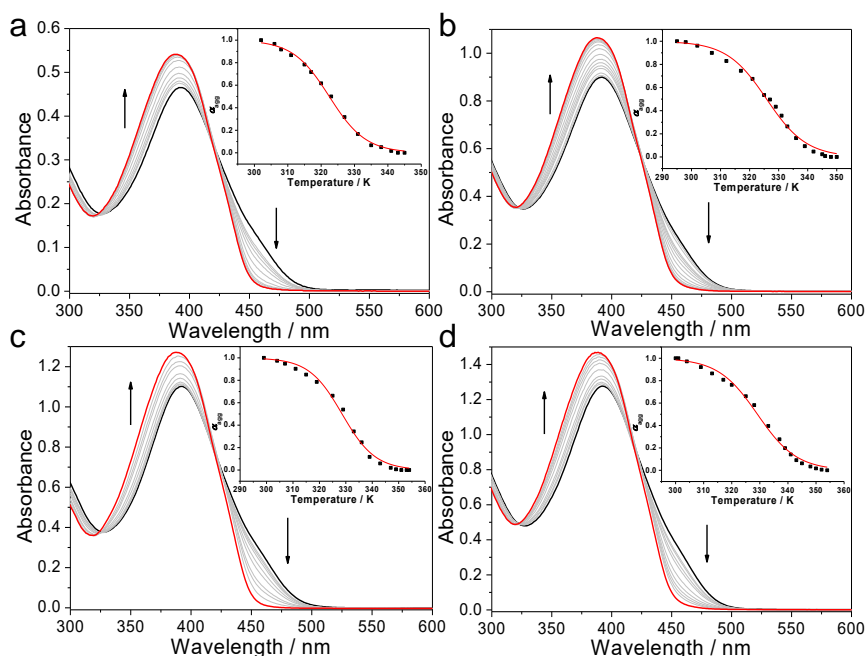


Figure S3. Temperature-dependent UV–Vis absorption spectra of **1**: a) 1.00×10^{-5} M; b) 2.00×10^{-5} M; c) 2.50×10^{-5} M; d) 3.00×10^{-5} M in MCH. Inset: α_{agg} as a function of temperature.

The normalized melting curves at $\lambda = 470$ nm display sigmoidal curves, which are characteristic for the isodesmic self-assembly mechanism. Non-linear fitting of the normalized curve affords the corresponding thermodynamic parameters (shown in Table S2).

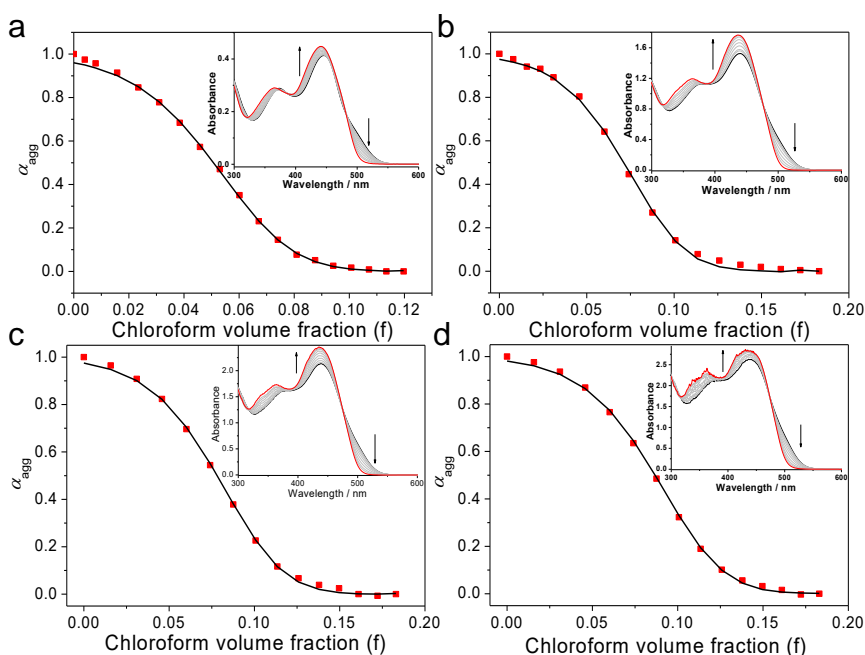


Figure S4. Degree of aggregation (α_{agg}) as a function of CHCl_3 volume fraction (f) monitored

at 515 nm: a) 1.00×10^{-5} M; b) 3.00×10^{-5} M; c) 5.00×10^{-5} M; d) 7.00×10^{-5} M in MCH. The black lines denote mathematical fitting of the curve according to the solvent-dependent equilibrium model (Equations S1–S4). Inset: solvent-dependent UV–Vis absorption spectra of **2**. The cooperativity parameter (σ) is determined to be 1, demonstrating the involvement of isodesmic mechanism for the self-assembly process of **2**. The detailed thermodynamic parameters are shown in Table S3.

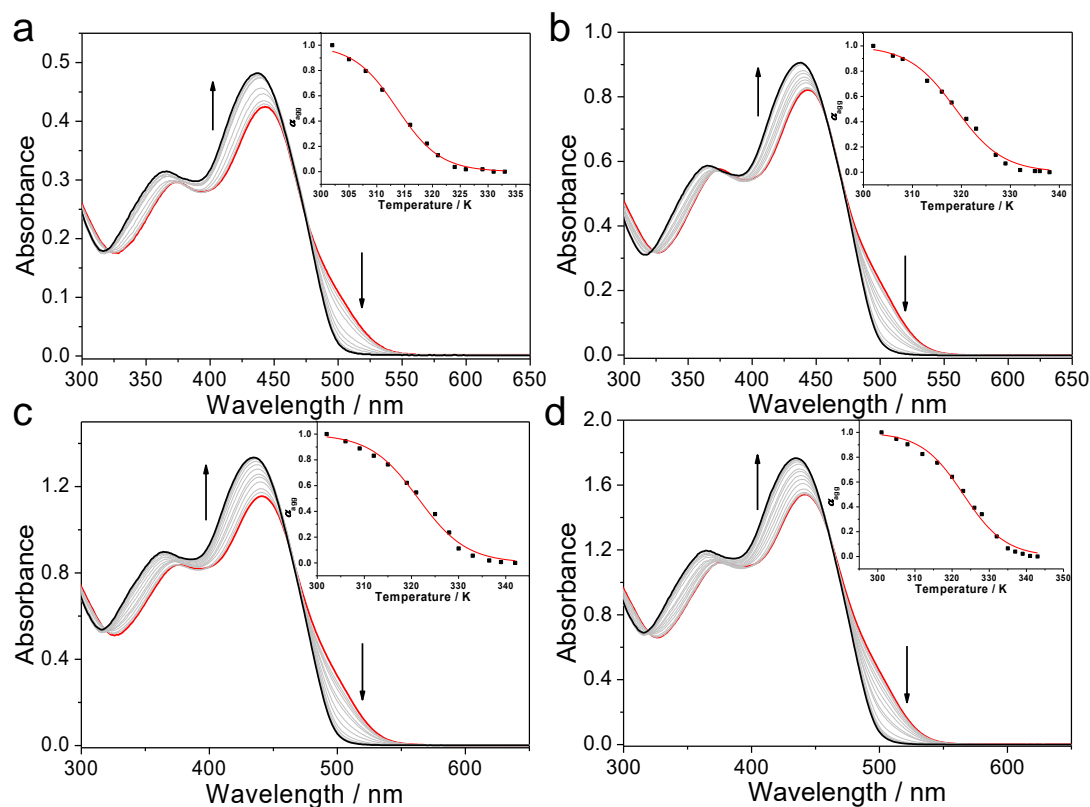


Figure S5. Temperature-dependent UV–Vis absorption spectra of **2**: a) 1.00×10^{-5} M; b) 2.00×10^{-5} M; c) 3.00×10^{-5} M; d) 4.00×10^{-5} M in MCH. Arrows indicate the spectral changes upon increasing temperature. Inset: α_{agg} as a function of temperature. The normalized melting curves at $\lambda = 515$ nm display sigmoidal curves, which are characteristic for the isodesmic assembling mechanism. Non-linear fitting of the normalized curve affords the corresponding thermodynamic parameters, as shown in Table S4.

Table S1. Thermodynamic parameters of the **1** self-assembly process, obtained by fitting the solvent-dependent UV–Vis absorption data

Concentration [mM]	0.01	0.02	0.03	0.04
$\Delta G^0 / \text{kJ}\cdot\text{mol}^{-1}$	−44.0	−44.5	−45.5	−47.0
$m / \text{kJ}\cdot\text{mol}^{-1}$	152	151	129	141
σ	1.0	1.0	1.0	0.90

Table S2. Thermodynamic parameters of the **1** self-assembly process, obtained by fitting the temperature-dependent UV–Vis absorption data in MCH

Concentration [mM]	T_e [K]	h_e [kJ mol ⁻¹]
0.01	322.43	-174.09
0.02	325.85	-141.85
0.025	328.57	-157.88
0.03	329.15	-141.71

Table S3. Thermodynamic parameters of the **2** self-assembly process, obtained by fitting the solvent-dependent UV–Vis absorption data

Concentration [mM]	0.01	0.03	0.05	0.07
ΔG^0 [kJ·mol ⁻¹]	-37.0	-36.5	-35.5	-35.5
m [kJ·mol ⁻¹]	166	137	123	120
σ	1.0	1.0	1.0	1.0

Table S4. Thermodynamic parameters of the **2** self-assembly process, obtained by fitting the temperature-dependent UV–Vis absorption data in MCH

Concentration [mM]	T_e [K]	h_e [kJ mol ⁻¹]
0.01	313.64	-231.40
0.02	318.84	-193.95
0.03	321.45	-185.31
0.04	323.05	-168.91

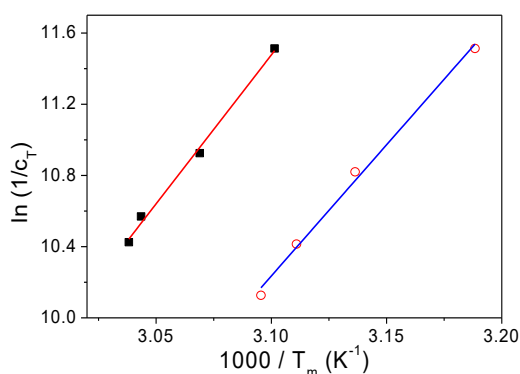


Figure S6. Van't Hoff plots for **1** (○) and **2** (■) in MCH. The red and blue lines denote the respective linear fitting curves. According to the modified Van't Hoff plot, ΔG^0 of the self-assembly process is lower of **2** than that of **1** (**2**: -35.8 kJ mol⁻¹ versus **1**: -40.6 kJ mol⁻¹).

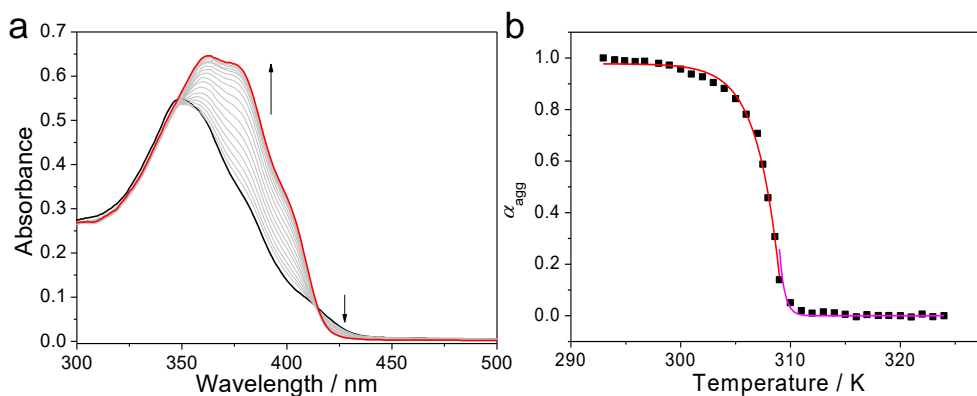


Figure S7. a) Temperature-dependent UV–Vis absorption spectra of **3** (1.00×10^{-5} M) in MCH. Arrows indicate the spectral changes upon increasing temperature. b) α_{agg} as a function of temperature monitored at 377 nm. It features a non-sigmoidal melting curve, denoting the adoption of nucleation–elongation mechanism. The lines denote the mathematical fitting of the curve according to the Meijer–Schenning–Van-der-Schoot model.

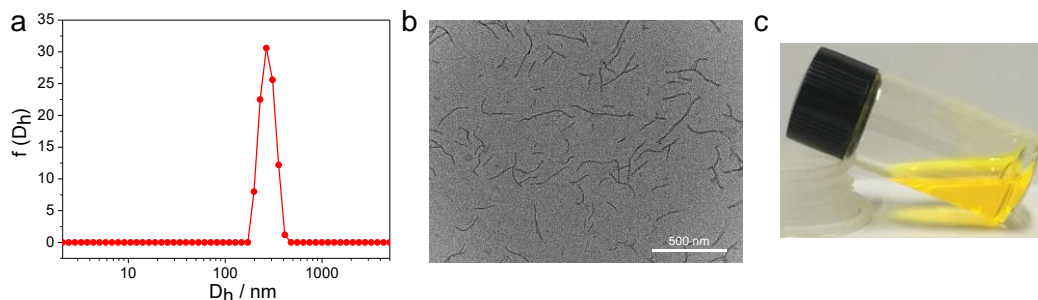


Figure S8. a) DLS measurements of **1** in MCH. b) TEM micrographs obtained by drop-casting the MCH solution of **1** on a copper grid. c) Images of solution from **1** (50 mM) in MCH at 293 K. **1** is prone to self-assemble into short nanofibers, with the averaged hydrodynamic diameter of 266 nm. No gel can be detected for **1**, even increasing the concentration to 50 mM.

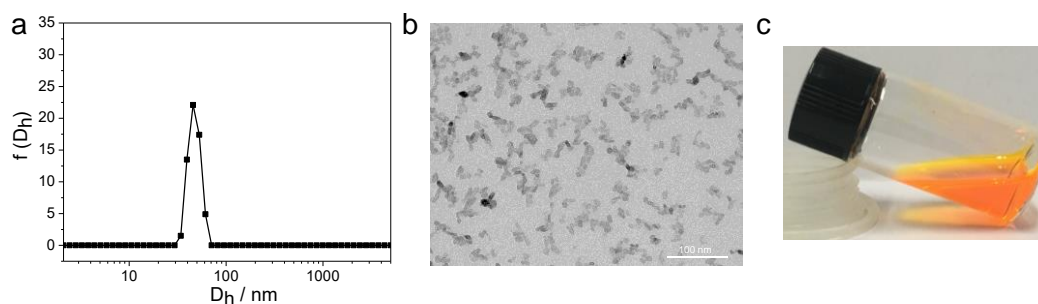


Figure S9. a) DLS measurements of **2** in MCH. b) TEM micrographs obtained by drop-casting the MCH solution of **2** on a copper grid. c) Images of solution from **2** (50 mM) in MCH at 293 K. **2** is prone to self-assemble into small nanoparticles, with the averaged hydrodynamic diameter of 46 nm. No gel can be detected for **2**, even increasing the concentration to 50 mM.

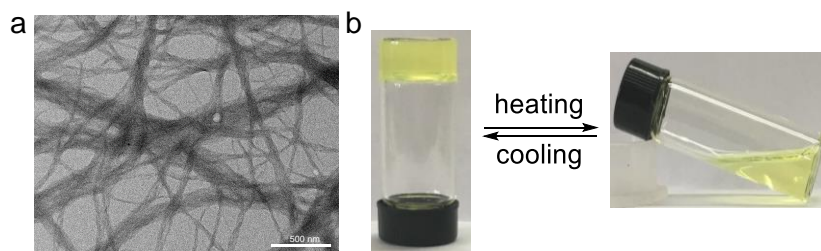


Figure S10. a) TEM micrographs obtained by dropping the MCH solution of **3** on a copper grid. b) Thermo-responsive gel–sol transition of **3** (1.00×10^{-2} M in MCH). **3** is prone to self-assemble into long fibers with several microns in length, and then entangle to form fibrous networks. When the monomer concentration of **3** exceeds 8 mM in MCH, it tends to form yellow transparent gels at room temperature.

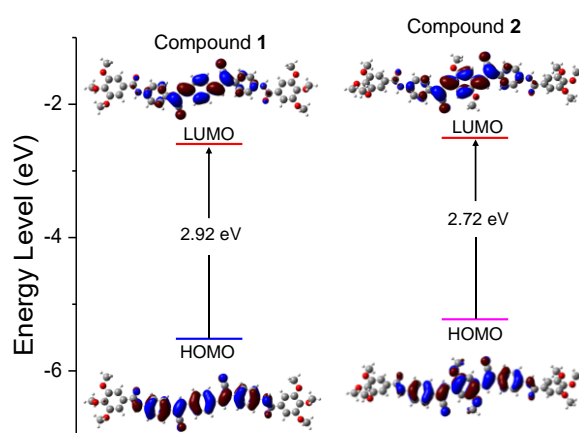


Figure S11. Energy-level diagram of **1** and **2** via TD-DFT computation. To avoid convergence difficulties, the energy levels in the diagram are obtained via DFT optimization in the gas phase. The electronic transition energy, oscillation strength, and oscillation contribution are obtained from TD-DFT computation in chloroform.

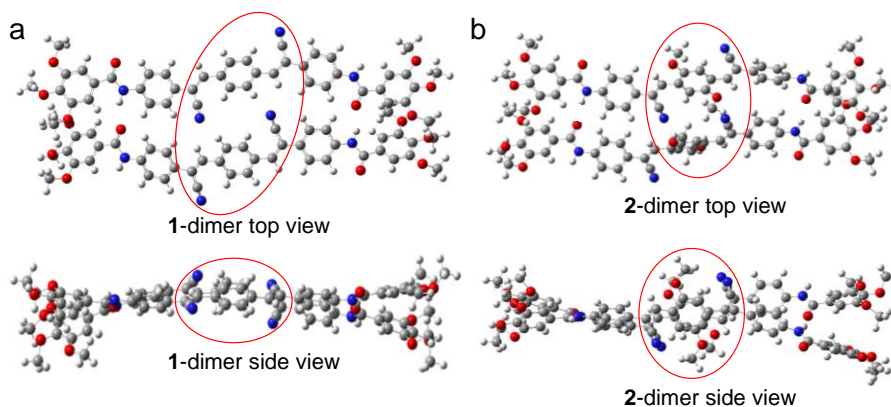


Figure S12. Optimized geometries of dimeric structures a) **1**-dimer and b) **2**-dimer, on the basis of DFT calculations at the level of B3LYP/6-31G(d). As can be seen from the top and side view of the dimeric structures **1**₂ and **2**₂, the two OCH₃ units bring more distorted conformation for the dicyanodistyrylbenzene unit, thus restricting close packing in the self-assembled structures.

4. Vapo-fluorochromism of 1–2 toward smart 3D code applications

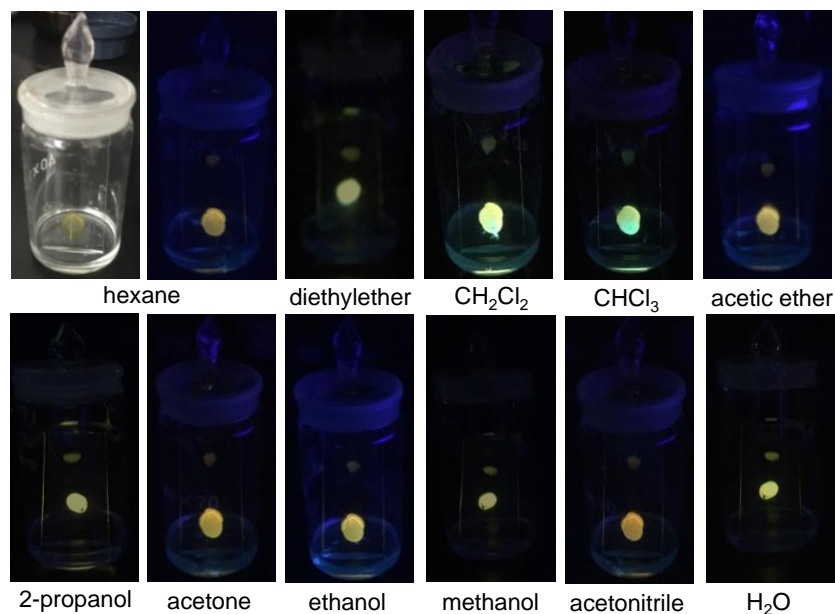


Figure S13. Photographs of vapo-fluorochromic experiments of **1**. The films of **1** are prepared by drop-casting its MCH solution onto the glass slide. When it is exposed to a series of solvent vapors, such as hexane, diethylether, dichloromethane, chloroform, acetic ether, 2-propanol, acetone, ethanol, methanol, acetonitrile, and water, resulting in distinct emission color change from orange to greenish-blue within seconds.

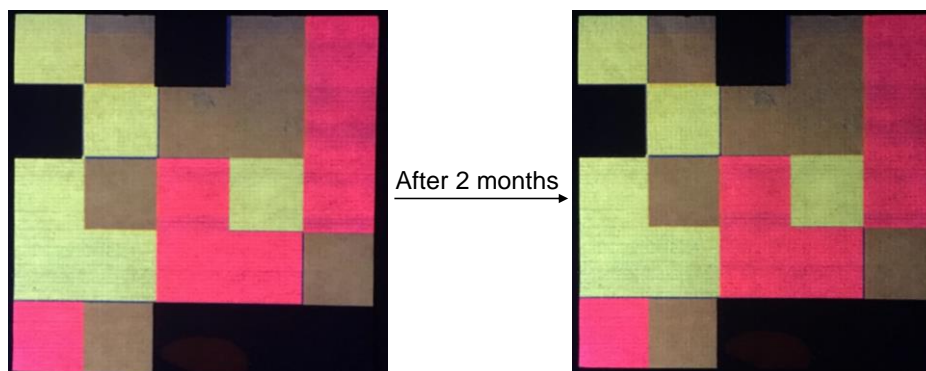
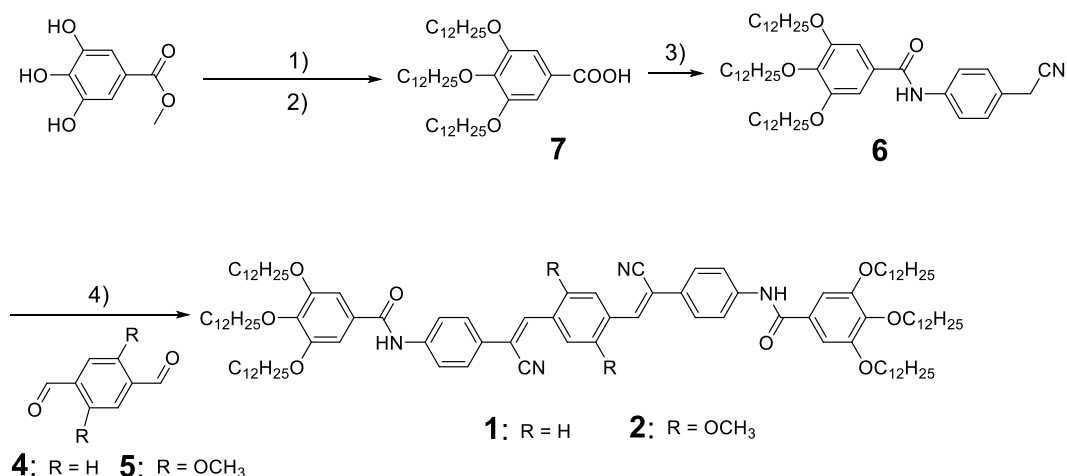
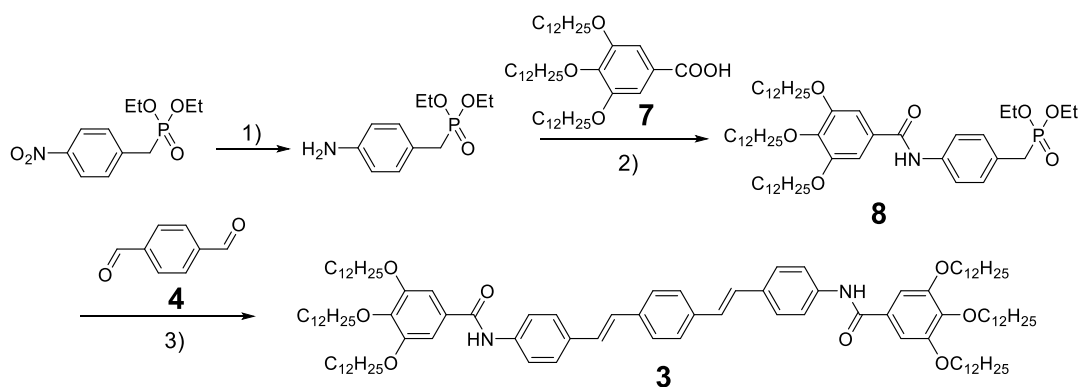


Figure S14. Photographs of fluorescent 3D code (size: 8×8 cm) on day 1 and after 2 months. The printed 3D code derived from **1–2** features sufficient stability and sustainability, since emission decay is scarcely detected upon placing under the ambient conditions for two months.

5. Synthetic routes to compounds 1–3



Scheme S1. Synthetic routes to the targeted compounds 1–2. 1) 1-bromododecane, CH₃CN, K₂CO₃, reflux; 2) ethanol, NaOH, reflux; 3) 2-(4-aminophenyl)acetonitrile, EDC, DMAP, CH₂Cl₂; 4) *t*-BuOH, *t*-BuOK.



Scheme S2. Synthetic route to compound 3. 1) SnCl₂•2H₂O, HCl, EtOH, reflux; 2) EDC, DMAP, CH₂Cl₂; 3) *t*-BuOK, THF.

4.1. Synthesis of 1

Compounds **6** (371 mg, 0.47 mmol) and **4** (30.0 mg, 0.22 mmol) were placed in 30 mL of *t*-BuOH, and stirred at 60 °C until completely dissolved. The *t*-BuOH solution (5 mL) of *t*-BuOK (35.0 mg, 0.31 mmol) was added to the reaction mixture. After stirring at 60 °C for 2 hours, the reaction mixture was evaporated to remove the solvent. The residue was purified by flash column chromatography (petroleum ether/CH₂Cl₂, 1 : 1 *v/v* as the eluent) to afford **1** as a yellow solid (300 mg, 80 %). ¹H NMR (300 MHz,

CDCl₃, room temperature) δ (ppm): 8.00 (s, 4H), 7.84 (s, 2H), 7.74 (q, $J = 9.1$ Hz, 8H), 7.54 (s, 2H), 7.06 (s, 4H), 4.04 (q, $J = 6.4$ Hz, 12H), 1.87–1.75 (m, 12H), 1.49 (s, 12H), 1.27 (s, 96H), 0.88 (t, $J = 6.5$ Hz, 18H). ¹³C NMR (75 MHz, CDCl₃) δ (ppm): 164.74, 152.25, 140.66, 138.54, 138.30, 134.37, 128.85, 128.68, 128.36, 125.79, 119.41, 116.80, 111.06, 104.77, 72.57, 68.42, 30.93, 30.92, 29.32, 28.75, 28.70, 28.65, 28.59, 28.41, 28.39, 28.37, 28.34, 25.08, 21.69, 13.12. MALDI-TOF-MS m/z : [M + H]⁺, C₁₁₀H₁₇₁N₄O₈, calculated 1677.3130; found 1677.3249.

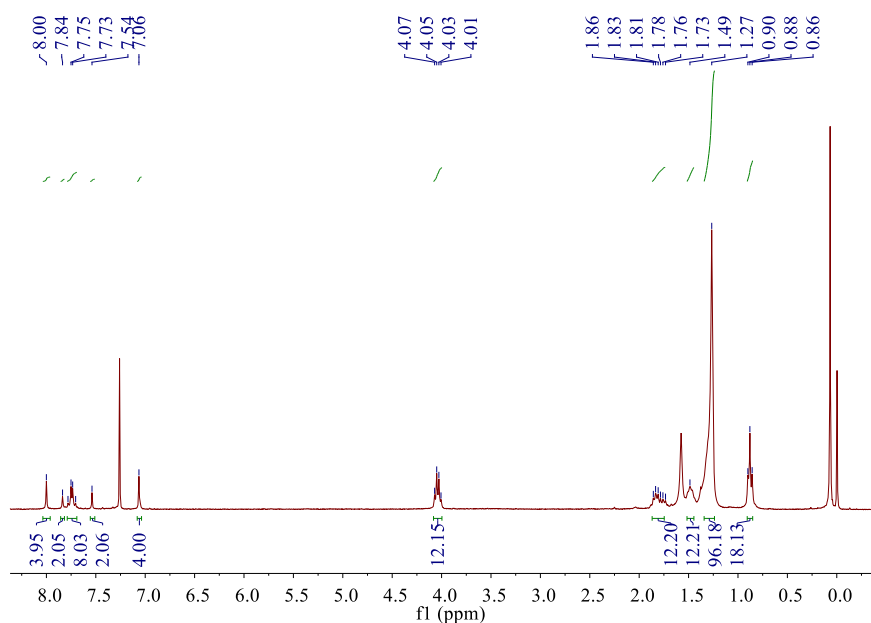


Figure S15. ¹H NMR spectrum (300 MHz, CDCl₃, room temperature) of **1**.

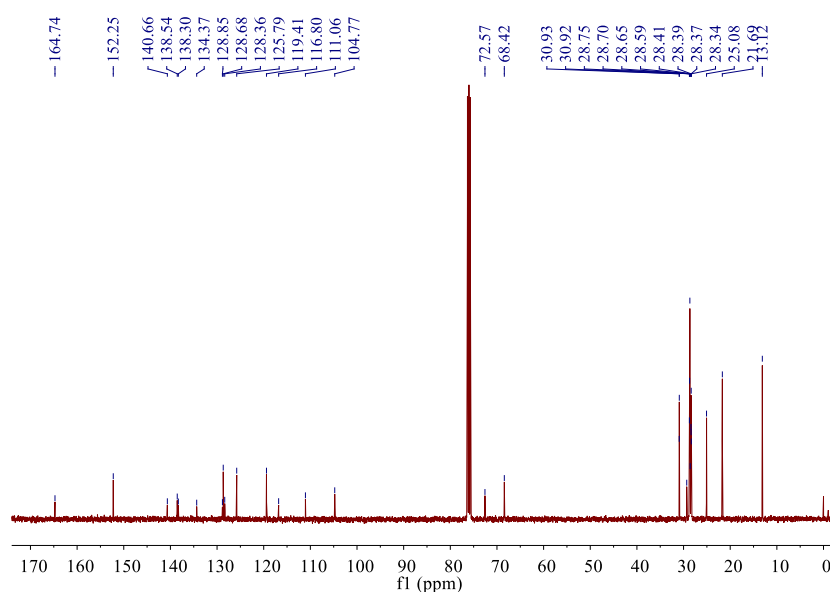


Figure S16. ¹³C NMR spectrum (75 MHz, DMSO-*d*₆, room temperature) of **1**.

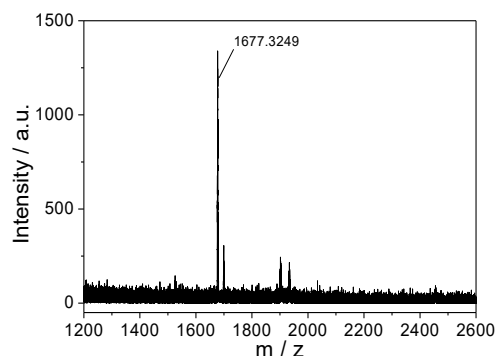


Figure S17. MALDI-TOF mass spectrum of **1**.

4.2. Synthesis of **2**

The synthetic procedure for **2** was similar to that for **1**, except that compound **5** was used instead of **4**. The product was obtained as an orange solid (195 g, 75%). ^1H NMR (300 MHz, CDCl_3) δ (ppm): 8.00 (s, 2H), 7.91 (s, 2H), 7.84 (s, 2H), 7.74 (s, 8H), 7.06 (s, 4H), 4.04 (dd, $J = 13.0, 6.5$ Hz, 12H), 3.98 (s, 6H), 1.88–1.73 (m, 12H), 1.49 (s, 12H), 1.27 (s, 96H), 0.88 (t, $J = 6.5$ Hz, 18H). ^{13}C NMR (75 MHz, CDCl_3) δ (ppm): 164.71, 152.27, 150.95, 140.71, 138.04, 133.76, 129.35, 128.45, 125.85, 124.44, 119.34, 117.36, 110.28, 109.16, 104.84, 72.58, 68.47, 55.33, 30.93, 30.92, 29.32, 28.74, 28.73, 28.70, 28.66, 28.65, 28.58, 28.41, 28.39, 28.36, 25.08, 21.68, 13.11. MALDI-TOF-MS m/z : $[\text{M} + \text{H}]^+$, $\text{C}_{112}\text{H}_{175}\text{N}_4\text{O}_{10}$, calculated 1736.3308; found 1736.3152.

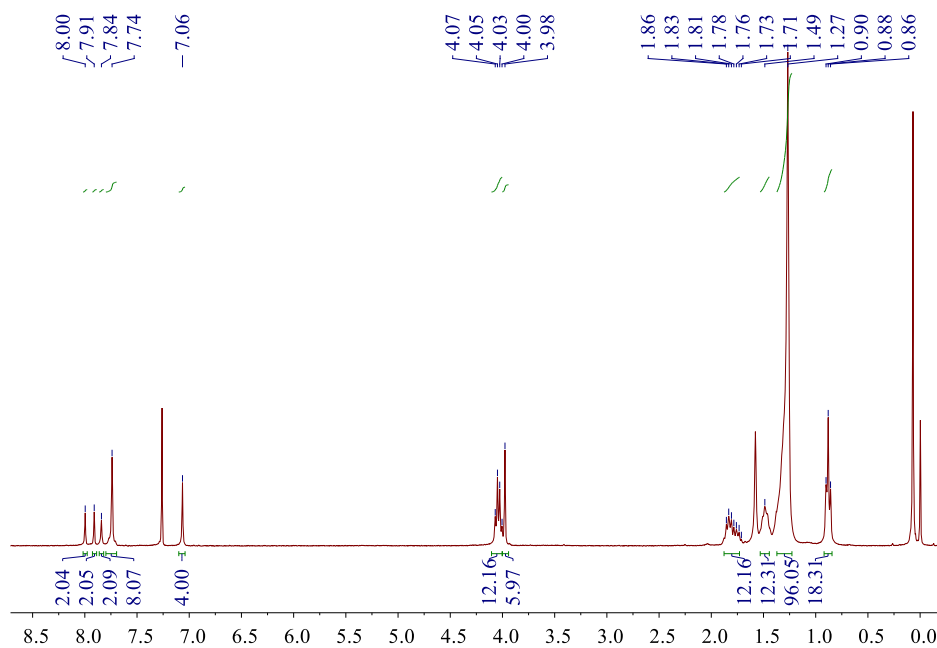


Figure S18. ^1H NMR spectrum (300 MHz, CDCl_3 , room temperature) of **2**.

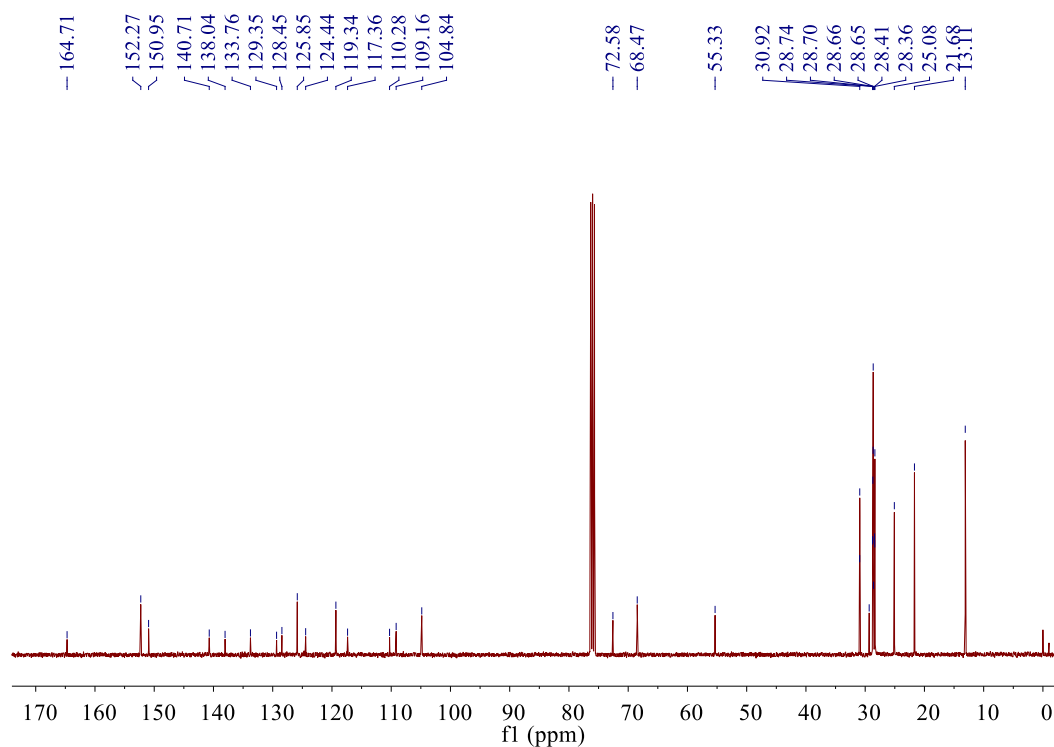


Figure S19. ^{13}C NMR spectrum (75 MHz, $\text{DMSO-}d_6$, room temperature) of **2**.

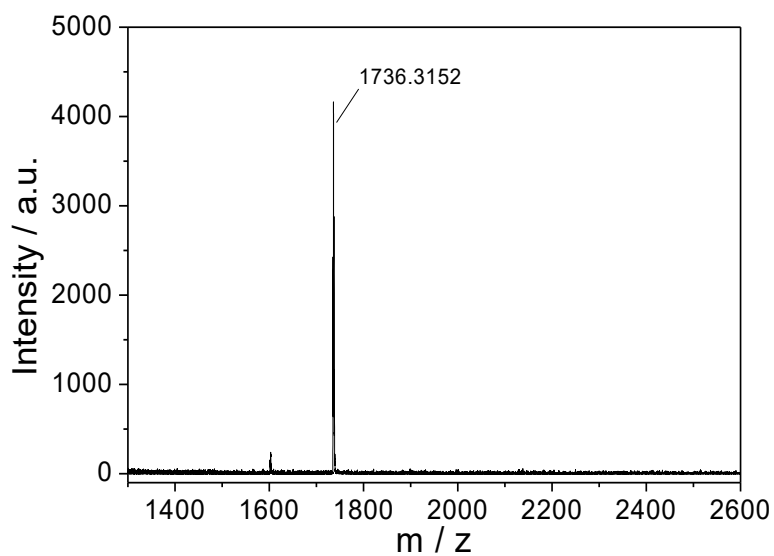


Figure S20. MALDI-TOF mass spectrum of **2**.

4.3. Synthesis of **3**

Compounds **8** (174 mg, 0.19 mmol) and **4** (12.0 mg, 0.09 mmol) were placed in 20 mL of THF, and stirred at room temperature for 30 minutes. The THF solution (5

mL) of *t*-BuOK (26.0 mg, 0.23 mmol) was added to the reaction mixture. After stirring at 70 °C for 12 hours, the reaction mixture was evaporated to remove the solvent, and the residue was extracted with H₂O/CH₂Cl₂ for three times. The combined organic extract was dried over anhydrous Na₂SO₄, and the solvent was removed with a rotary evaporator. The residue was purified by flash column chromatography (ethyl acetate /CH₂Cl₂, 1 : 9 v/v as the eluent) to afford **3** as a pale-yellow solid (104 mg, 70 %). ¹H NMR (300 MHz, CDCl₃, room temperature) δ (ppm): 7.86 (d, *J* = 12.4 Hz, 2H), 7.70–7.60 (m, 4H), 7.58–7.47 (m, 6H), 7.42–7.28 (m, 2H), 7.17 (dd, *J* = 19.9, 7.8 Hz, 2H), 7.09 (d, *J* = 3.2 Hz, 2H), 7.04 (d, *J* = 6.3 Hz, 4H), 6.57 (d, *J* = 6.3 Hz, 1H), 4.02 (t, *J* = 6.2 Hz, 12H), 1.77 (dd, *J* = 18.7, 7.3 Hz, 13H), 1.50–1.43 (m, 12H), 1.27 (s, 96H), 0.87 (d, *J* = 6.9 Hz, 19H). ¹³C NMR (75 MHz, CDCl₃) δ (ppm): 164.61, 152.22, 140.50, 136.45, 135.62, 132.60, 128.81, 126.16, 125.75, 119.24, 104.78, 72.55, 68.43, 30.92, 28.64, 28.36, 25.07, 21.68, 13.11. MALDI-TOF-MS *m/z*: [M + H]⁺, C₁₀₈H₁₇₃N₂O₈, calculated 1626.3192; found 1626.3056.

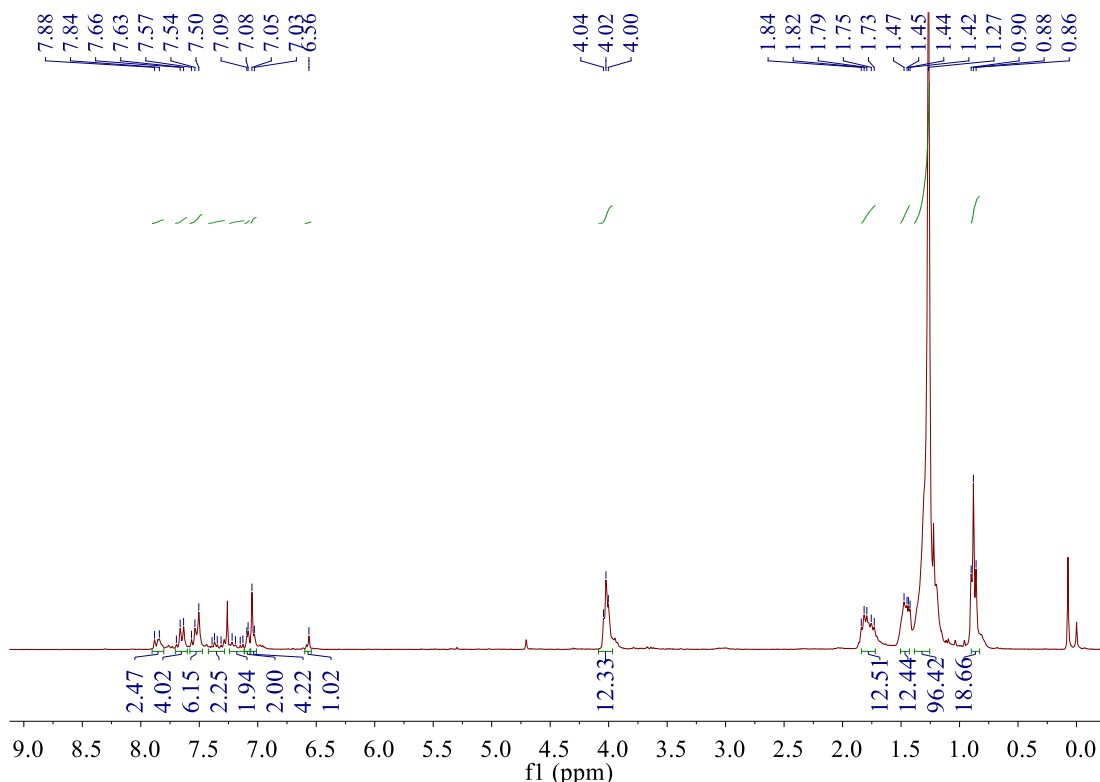


Figure S21. ¹H NMR spectrum (300 MHz, CDCl₃, room temperature) of **3**.

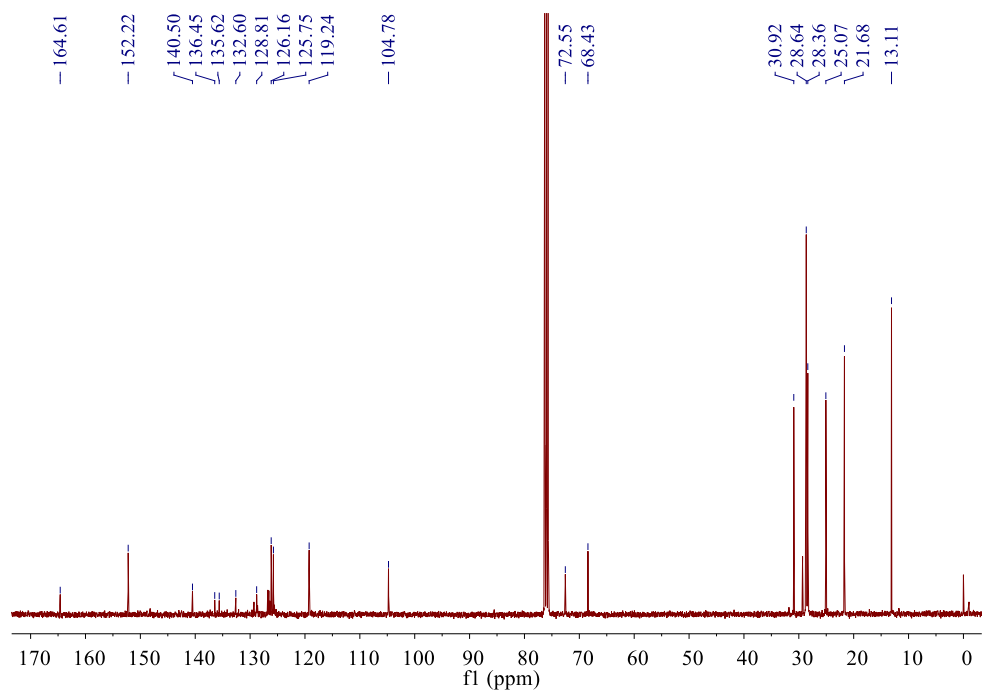


Figure S22. ^{13}C NMR spectrum (75 MHz, CDCl_3 , room temperature) of **3**.

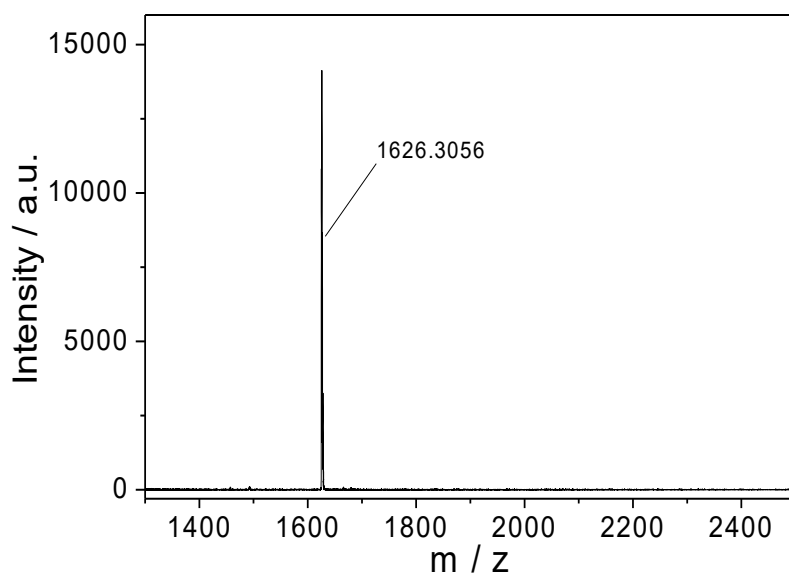


Figure S23. MALDI-TOF mass spectrum of **3**.

References:

- S1. C. Choong, J. S. Foord, J.-P. Griffiths, E. M. Parker, L. Baiwen, M. Bora, M. G. Moloney, *New J. Chem.*, **2012**, *36*, 1187–1200.
- S2. Q. Sun, C.-W. Fu, B. Aguila, J. Perman, S. Wang, H.-Y. Huang, F.-S. Xiao, S. Ma, *J. Am. Chem. Soc.*, **2018**, *140*, 984–992.
- S3. O. Simalou, R. Lu, P. Xue, P. Gong, T. Zhang, *Eur. J. Org. Chem.*, **2014**, 2907–2916.
- S4. S. Das, N. Okamura, S. Yagi, A. Ajayaghosh, *J. Am. Chem. Soc.*, **2019**, *141*, 5635–5639.
- S5. Gaussian 09, Revision A.02, M. J. Frisch, G. W. Trucks, H. B. Schlegel, G. E. Scuseria, M. A. Robb, J. R. Cheeseman, G. Scalmani, V. Barone, B. Mennucci, G. A. Petersson, H. Nakatsuji, M. Caricato, X. Li, H. P. Hratchian, A. F. Izmaylov, J. Bloino, G. Zheng, J. L. Sonnenberg, M. Hada, M. Ehara, K. Toyota, R. Fukuda, J. Hasegawa, M. Ishida, T. Nakajima, Y. Honda, O. Kitao, H. Nakai, T. Vreven, J. A. Montgomery, Jr., J. E. Peralta, F. Ogliaro, M. Bearpark, J. J. Heyd, E. Brothers, K. N. Kudin, V. N. Staroverov, R. Kobayashi, J. Normand, K. Raghavachari, A. Rendell, J. C. Burant, S. S. Iyengar, J. Tomasi, M. Cossi, N. Rega, J. M. Millam, M. Klene, J. E. Knox, J. B. Cross, V. Bakken, C. Adamo, J. Jaramillo, R. Gomperts, R. E. Stratmann, O. Yazyev, A. J. Austin, R. Cammi, C. Pomelli, J. W. Ochterski, R. L. Martin, K. Morokuma, V. G. Zakrzewski, G. A. Voth, P. Salvador, J. J. Dannenberg, S. Dapprich, A. D. Daniels, O. Farkas, J. B. Foresman, J. V. Ortiz, J. Cioslowski, and D. J. Fox, *Gaussian, Inc., Wallingford CT*, **2009**.
- S6. M. M. J. Smulders, M. K. L. Nieuwenhuizen, T. F. A. de Greef, P. van der Schoot, A. P. H. J. Schenning, E. W. Meijer, *Chem. Eur. J.*, **2010**, *16*, 362–367.
- S7. P. Jonkheijm, P. van der Schoot, A. P. H. J. Schenning, E. W. Meijer, *Science*, **2006**, *313*, 80–83.
- S8. P. A. Korevaar, C. Schaefer, T. F. A. de Greef, E. W. Meijer, *J. Am. Chem. Soc.*, **2012**, *134*, 13482–13491.